ACSNANO

www.acsnano.org

ARTICLE

Origins of Fermi Level Pinning for Ni and Ag Metal Contacts on Tungsten Dichalcogenides

Xinglu Wang, Yaoqiao Hu, Seong Yeoul Kim, Rafik Addou, Kyeongjae Cho, and Robert M. Wallace*

Cite This: https://doi.org/10.1021/acsnano.3c06494 Read Online

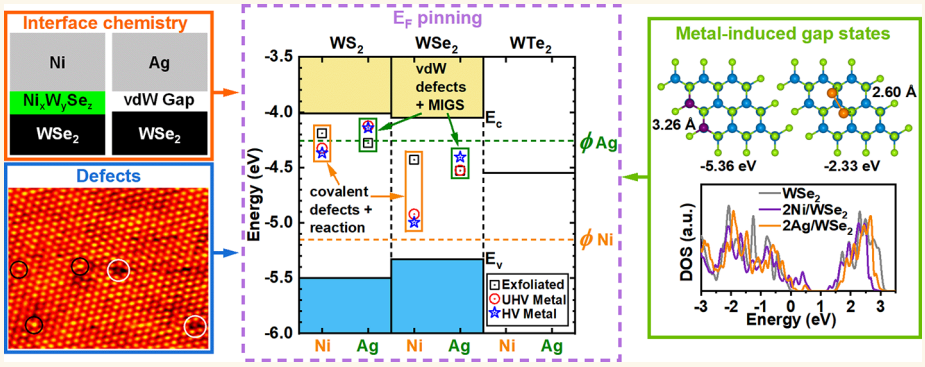

ABSTRACT: Tungsten transition metal dichalcogenides (W-TMDs) are intriguing due to their properties and potential for application in next-generation electronic devices. However, strong Fermi level (E_F) pinning manifests at the metal/W-TMD interfaces, which could tremendously restrain the carrier injection into the channel. In this work, we illustrate the origins of E_F pinning for Ni and Ag contacts on W-TMDs by considering interface chemistry, band alignment, impurities, and imperfections of W-TMDs, contact metal adsorption mechanism, and the resultant electronic structure. We conclude that the origins of E_F pinning at a covalent contact metal/W-TMD interface, such as Ni/W-TMDs, can be attributed to defects, impurities, and interface reaction products. In contrast, for a van der Waals contact metal/TMD system such as Ag/W-TMDs, the primary factor responsible for E_F pinning is the electronic modification of the TMDs resulting from the defects and impurities with the minor impact of metal-induced gap states. The potential strategies for carefully engineering the metal deposition approach are also discussed. This work unveils the origins of E_F pinning at metal/TMD interfaces experimentally and theoretically and provides guidance on further enhancing and improving the device performance.

KEYWORDS: *metal contact, transition metal dichalcogenides, Fermi level pinning, interface chemistry, band alignment, imperfections, density functional theory*

INTRODUCTION

Transition metal dichalcogenides (TMDs) have demonstrated immense potential for applications in state-of-the-art electronic, optoelectronic, and spintronic devices because of their outstanding electronic, optical, mechanical, and magnetic properties.[1−7] However, the failure of tuning the Schottky barrier height (SBH) by the work function (Φ) of metal contacts strongly limits the efficiency of carrier injection and hence the electronic performance of TMD-based devices.[8−11] Several strategies, such as the use of interlayer,[12−18] phase engineering,[19,20] surface or chemical doping,[21−24] and transferred or buffered van der Waals (vdW) metal contacts,[25,26] have been employed to alleviate the E_F pinning effect and to reduce the contact resistance (R_c) at the source and drain contacts. Nevertheless, the front- and back-end-of-line (FEOL and BEOL) processes for wafer scale integration necessitate direct metallization of the TMD-based devices. Employing direct metallization, various metal contacts (Ti, Au, Pd, Pt, Sc, Cr, Ir, Al, Ag, In, Y, Ni, Sn, Mo, Bi, Sb, etc.) have been employed to investigate their contact performance with TMDs;[8,9,26−35] however, the mechanism of the strong E_F pinning effect at the metal/TMD interface remains elusive in the aspect of fundamental science.

Received: July 14, 2023
Accepted: September 29, 2023

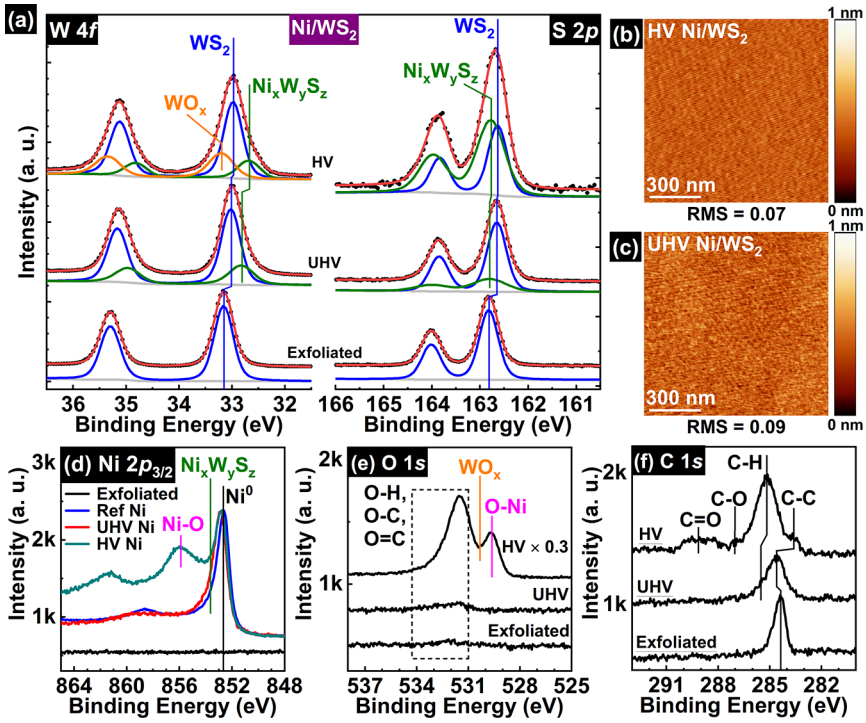

Figure 1. (a) W 4*f* and S 2*p*, (d) Ni $2p_{3/2}$, (e) O 1*s*, and (f) C 1*s* spectra of WS_2 bulk crystal surfaces following exfoliation and subsequent Ni depositions under UHV and HV conditions, as well as AFM images of Ni/WS_2 bulk crystal surfaces deposited under (b) HV and (c) UHV conditions. The unit of the root-mean-square (RMS) is nm.

Many efforts have been spent to understand the origin of E_F pinning from several perspectives. English et al. have reported that the R_c can vary significantly with the deposition conditions for TMD-based devices.[36] Interface chemistry studies unveil that the contact performance can be improved by carefully reducing the impingement rate of the background gases on the TMD substrate during the metal deposition process.[30,31,37] The oxidation of the contact metal and its contact interface with TMD substrates could strongly modify the intrinsic interface chemistry and lead to degraded contact performance.[37,38] In addition, the contact resistance can be reduced by more than 2 magnitudes if the air and water exposure can be minimized during the metalization of the contacts.[39] It has also been unveiled that minimizing the TMD transfer holding polymer residue can significantly improve the $I_{on/off}$ ratio and decrease the contact resistance.[25,40] These discoveries indicate the importance of careful control of the processing conditions of the TMD transistors.

Besides the processing conditions, the properties and quality of a semiconductor TMD can also impact the nature of the metal/TMD interface. Addou et al. have reported that the intrinsic imperfections of TMDs could induce gap states and vary the Φ of TMDs after exfoliation.[41,42] For example, S vacancy can introduce gap states 0.04−0.5 eV below the conduction band minimum, which is an n-type dopant to the MoS_2.[43] Other imperfections, such as antisites and impurities, can cause heterogeneous doping on the same freshly exfoliated surface of TMDs.[44] Furthermore, the interaction between the imperfections and the adsorbed contact metal atoms could cause orbital hybridization, leading to the formation of unexpected bonds and interface states.[44,45] These alterations would change the band alignment and the SBH substantially at the metal/TMD interface.

Recently, theory calculations predicted that the contact metal adsorption site and orientation can be tuned to lower the SBH on the TMDs. In those studies, Moiré pattern adsorption configurations enable greater Fermi level depinning than other geometries without a twisted angle on the TMDs.[46,47] This finding indicates that the adsorption mechanism of the metal atoms on the TMD surface is essential in tuning the SBH and achieving an Ohmic contact.

From the above, it can be inferred that the origin of E_F pinning cannot be solely explained from a single aforementioned perspective. For a specific metal/TMD interface, the E_F pinning effect at a metal/TMD interface may emerge from an integration of various components, which is further bolstered by the scattered R_c values reported from different research groups even with the same metal and TMD combination.[48] This brings up a strong demand for the investigation of fundamental science and the weight of each component. This complication of the coexisted components necessitates a dedicated systematic and comprehensive study to understand the essential physics and chemistry that lead to the E_F pinning of metal contacts on TMDs.

Among the W-TMDs, WS_2 and WSe_2 have attracted great attention due to their low subthreshold slope (down to 60 mV/dec), moderate mobility (250 $cm^2/V{\cdot}s$), and high I_{on}/I_{off} ratio (up to ∼10^9).[10,29,49−52] WTe_2 shows promise in being used as an atomically thin high current interconnect and an interlayer between metal contacts and TMDs to improve the electrical performance.[53,54] For the contact metals, Ni and Ag have demonstrated great potential in achieving a low R_c on TMDs. More specifically, Ni has demonstrated promising R_c values of 500 and 700 Ω·μm on MoS_2 and WS_2, respectively.[24,39] Ag has shown an extremely low R_c of 180 Ω·μm with MoS_2 upon direct metal deposition.[55] However, the physical and chemical properties of the interfaces of Ni and

https://doi.org/10.1021/acsnano.3c06494
ACS Nano XXXX, XXX, XXX−XXX

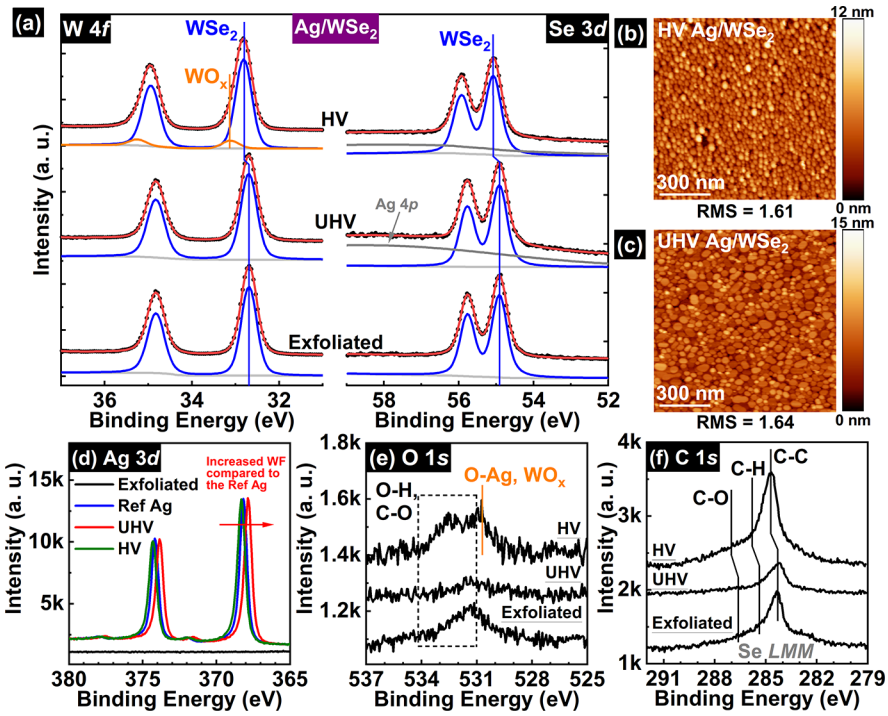

Figure 2. (a) W 4*f* and Se 3*d*, (d) Ag 3*d*, (e) O 1*s*, and (f) C 1*s* spectra of WSe_2 bulk crystal surfaces following exfoliation and subsequent Ag depositions under UHV and HV conditions, as well as AFM images of Ni/WS_2 bulk crystal surfaces deposited under (b) HV and (c) UHV conditions. The unit of the RMS is nm.

Ag metal contacts with W-TMDs, which is the key to achieving Ohmic contacts with low R_c,[26] have not been studied systematically. It has been unveiled that Ni and Ag form covalent and van der Waals (vdW) interfaces with MoS_2, respectively.[56] The distinct interface types, together with their outstanding contact performance, make them perfect candidates to understand the origin of E_F pinning by comparing the two cases under the same processing conditions.

To study the contact type (Schottky or Ohmic, covalent, or vdW) between exfoliated W-TMD bulk crystals and Ni or Ag contacts, the interface chemistry, band alignment, and surface morphology of Ni and Ag contacts on W-based TMDs are investigated by X-ray photoelectron spectroscopy (XPS) and atomic force microscopy (AFM). The impact of deposition ambient is studied by employing *in situ* ultrahigh vacuum (UHV) and *ex situ* high vacuum (HV) deposition conditions. The use of HV deposition methods is common in the majority of materials and device research laboratories, and thus, the literature is replete with such deposition methods employing TMDs. As noted above, reports have indicated that the deposition ambient can be important in the context of contact resistance.[36−39] Comparing a typical ambient deposition (HV) with a well-controlled ambient ~~ambient~~ (UHV) enables the discrimination of reaction products that are likely present in a contact formed under HV conditions. The effect of imperfections, such as defects and impurities, of TMDs on the E_F pinning is characterized by scanning tunneling microscopy/spectroscopy (STM/STS). The contact metal atom adsorption mechanism is studied by density functional theory (DFT) and is correlated to the interface chemistry and surface morphology. The implications of the resultant interface chemistry, band alignment, and electronic effect of the imperfections and the adsorbed metal atoms on the contact performance are demonstrated. Potential strategies for optimizing the direct metal deposition process are discussed.

RESULTS

Ni Reduction of W-Based TMDs. The W 4*f* and S 2*p* spectra of WS_2 bulk crystal before and after ∼1 nm Ni deposition in UHV and HV are shown in Figure 1a. The emergence of an additional $Ni_xW_yS_z$ intermetallic state indicates the reaction between Ni and WS_2 after Ni deposition. Smooth surfaces (RMS roughness <0.1 nm) obtained after Ni deposition under HV and UHV conditions are shown in Figures 1b and c, respectively. This result also suggests the Ni reduction of WS_2 at the Ni/WS_2 interface. WO_x is detected after Ni deposition under HV conditions in the W 4*f* spectra. The water and OH residuals in the HV chamber as well as the air exposure during the *ex situ* transfer process likely lead to oxidation of the Ni/WS_2 interface. The oxidation of the Ni/WS_2 interface is further evident by the detection of Ni oxide bonding in the Ni $2p_{3/2}$ and the O 1*s* spectra after Ni deposition under HV conditions as shown in Figures 1d and e. Adventitious carbon species are detected before and after Ni deposition in UHV and HV. They likely originate from the carbon tape and the outgassed carbon species from the heated Ni source. However, the absence of any metal carbide features (∼282 eV) after Ni deposition demonstrates that the involvement of carbon in the interface reaction is below the detection limit of XPS.

The interface reaction at the Ni/WSe_2 and Ni/WTe_2 interfaces is congruent with that of the Ni/WS_2 interface. The Ni reduction of WSe_2 (WTe_2) and the formation of $Ni_xW_ySe_z$ ($Ni_xW_yTe_z$) are detected after Ni deposition under UHV and HV conditions. The core level spectra and relevant discussion are displayed in the Supporting Information.

https://doi.org/10.1021/acsnano.3c06494
ACS Nano XXXX, XXX, XXX−XXX

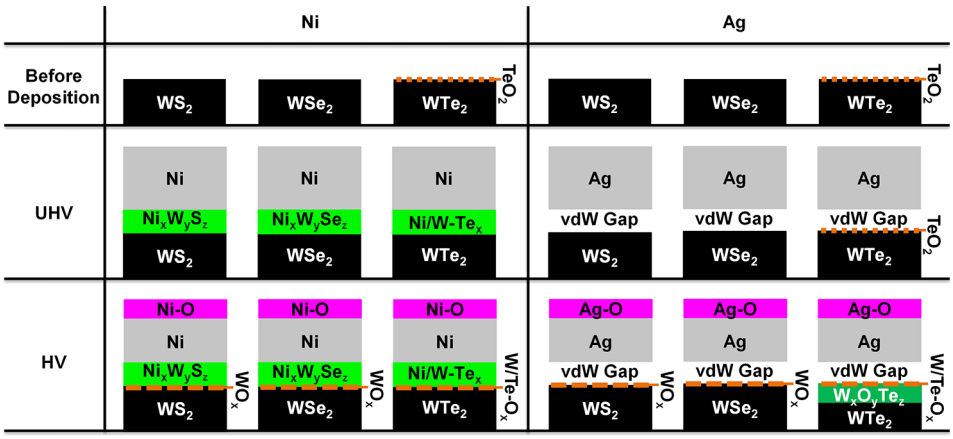

Figure 3. Schematics of the interfaces between contact metals (Ni and Ag) and W-TMDs before and after metal depositions in UHV and HV.

vdW Gap between Ag and W-TMDs. The interface chemistry of Ag/W-TMD interfaces with different chalcogen atoms is similar regarding interface reactions after Ag deposition under both UHV and HV conditions. Therefore, in this section, Ag/WSe_2 is chosen as the representative case to discuss the interface chemistry upon Ag deposition. The core level spectra and relevant discussion of Ag/WS_2, and Ag/WTe_2 are presented in the Supporting Information.

Any additional intermetallic chemical state is absent in the W 4*f* and Se 3*d* spectra after Ag depositions in UHV and HV as shown in Figure 2a. This indicates the persistence of WSe_2 and the formation of a vdW contact for the Ag/WSe_2 interface. The full width at half-maximums (fwhm's) of the W-TMD bulk crystal and Ag metal states stay almost the same after Ag deposition as shown in Table S1 to S4. This result indicates that the core level orbital interaction between Ag and W-TMDs is below the detection limit of XPS, confirming the formation of a vdW interface between Ag and W-TMDs. The Ag islands formation on the WSe_2 surfaces indicates the Volmer–Weber growth of Ag film on the WSe_2 bulk surfaces under UHV and HV conditions as shown in Figure 2b and c. This finding is congruent with the formation of a vdW gap between Ag and WSe_2. In Figure 3d, the Ag 3*d* peaks of the UHV samples shift to a lower binding energy compared to the reference Ag. This indicates that the Φ of the 1 nm Ag film deposited under the UHV condition is greater than that of the ~30 nm reference Ag film. Wood has predicted that the Φ of a small metal sphere should be smaller than that of a planar metal film,[57] which has also been reported to occur on MoS_2 in UHV.[56] However, for the Ag islands deposited on WSe_2, the Φ value is greater than the Φ value of the reference Ag film. This suggests the formation of interface dipole at the Ag/WSe_2 interfaces, which is likely due to the charge redistribution around the intrinsic defects of WSe_2 bulk.[11,41,42] For the Ag islands deposited under HV conditions, the sizes of the islands are smaller and more uniform than those of the islands deposited under UHV conditions. This possibly originates from the oxidation of the Ag/WSe_2 interface deposited under HV conditions as indicated by the appearance of Ag and W oxides in the W 4*f* and O 1*s* spectra. The oxidation of Ag also contributes to the positive shift of the Ag 3*d* peaks of the HV sample. In Figure 2f, the C 1*s* spectra overlap with the Se *LMM* auger spectra as indicated by the shakeup around 285 eV. The metal carbide bonds are below the detection limit of XPS for the Ag/WSe_2 samples after Ag deposition in UHV and HV. This finding demonstrates that the bonding of carbon in the interface reaction is not detectable for the Ag/WSe_2 samples deposited under UHV and HV conditions.

The interfaces of Ni and Ag with W-TMDs are summarized in Figure 3. The interface type is consistent for W-TMDs regardless of the ~~number of~~ chalcogen atoms for a specific contact metal. Ni forms covalent interfaces on W-TMDs with the formation of intermetallic reaction products. In contrast, Ag forms vdW gaps on W-TMDs without detectable interface reactions. Oxidation of the contact metal films is detected on the HV samples, which highlights the importance of carefully controlling the processing conditions for metallization.

Band Alignment and Fermi Level Pinning. The band alignment of the metal/TMD interfaces is calculated from the shifts of TMD bulk crystal states in the W 4*f* spectra referring to the peak positions in the references.[30,31,37] Specifically, the W $4f_{7/2}$ peaks of WS_2 and WSe_2 in Table S5 are used to extract the binding energy shift before and after metal deposition in UHV and HV. A negative shift of the bulk crystal chemical state in the W 4*f* spectra indicates a negative shift in the valence band maximum spectra. This means that the E_F shifts toward the vacuum level, which indicates the decrease of the Φ.[58] The details of the band alignment extraction method can be found in Figure S8. 1T′-WTe_2 investigated in this study is semimetallic. Accordingly, this Φ is aligned with the Φ of the XPS system spectrometer. Therefore, the binding energy variation upon metal deposition should be below the energy resolution of XPS. This identical data analysis process readily enables a direct comparison with the previous band alignment results.[30,31,37,45,59,60] In Figure 4, the energy position of the E_Fs obtained from the *in situ* UHV samples are considered the *true* values compared to the HV samples because any contamination from the ambient HV and the following *ex situ* process could introduce deviations to the measured results for the HV samples. E_Fs extracted from the HV samples are also shown for comparison. The variability of the E_F before metal depositions is due to the inhomogeneous distribution of its impurities and defects.[44,96]

The E_F of the Ni/WS_2 interface is pinned at −4.33 eV (relative to the vacuum level), leading to a Schottky barrier height of 0.32 eV for electron injection.[31] The E_F of the Ni/WS_2 interface after Ni deposition in UHV is close to the E_F of WS_2 (−4.19 eV) before metal deposition. The doping effect of TMDs caused by their defects impurities has been reported to give rise to the modulation of the E_F position.[41,42,44] This

https://doi.org/10.1021/acsnano.3c06494
ACS Nano XXXX, XXX, XXX−XXX

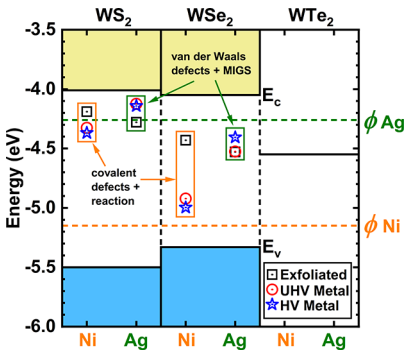

Figure 4. Band alignment of contact metal/W-TMDs interfaces before and after metal depositions in UHV and HV. The energy scale is relative to the vacuum level. The contact type (covalent or vdW) and the main origin of E_F pinning are also shown in this figure.

doping effect concurrent with the formation of the $Ni_xW_yS_z$ intermetallic probably dominates the E_F pinning at the Ni/WS_2 interface according to the interface chemistry study. The Schottky barrier height for the Ag/WS_2 interface is 0.11 eV as shown in Figure 4. Considering that the interface reaction between Ag and WS_2 is below the detection limit of XPS and the E_F after Ag deposition is close to the intrinsic E_F of WS_2, the doping effect caused by the defects and impurities of WS_2 likely leads to the E_F pinning at the Ag/WS_2 interface. The formation of an interface dipole and the appearance of gap states could partially explain the E_F pinning as reported by DFT calculation results.[11] Since the E_F of the Ag/WS_2 interface is close to the Φ of Ag, it is also possible that the Ag/WS_2 interface follows the Schottky−Mott rule.

The WSe_2 after exfoliation is n-type, which is probably due to the impurities, like In, Cu, and alkali metals, detected by inductively coupled plasma mass spectrometry (ICP-MS).[61,62] Impurities such as Re, Ag, and halogens, which are below the detection limit of ICP-MS for this sample, are also reported to induce n-type doping to TMDs.[21,63−66] Very recently, Stolz et al. have reported that vanadium is a p-type dopant for WSe_2 synthesized by metalorganic chemical vapor deposition.[67] It has been highlighted that the E_F pinning and Schottky contact behavior show up upon the number of WSe_2 layers exceeding 2 due to the change of the band structure.[67] This affirms that the impurity dopant is one of the origins of E_F pinning at the metal/TMD interface. The E_F of Ni/WSe_2 is pinned at 4.92 eV which is close to the valence band edge of the WSe_2 bulk crystal (5.33 eV). Therefore, Ni could potentially serve as a p-type contact for the WSe_2-based devices. The E_F of the Ni/WSe_2 interface is much closer to the Φ of Ni metal (further away from the intrinsic E_F of TMDs) than that of the Ni/WS_2 interface. This finding suggests that the E_F pinning effect from the interface reduction reaction products is more dominant for the Ni/WSe_2 interface, which means that the defects and impurities of WSe_2 contribute less to the E_F pinning compared to that of WS_2. The E_F for the Ag/WSe_2 interface is pinned at the same energy position as the intrinsic E_F of WSe_2 before metal deposition. This finding indicates that the intrinsic defects dominate the E_F pinning for the Ag/WSe_2 interface. The E_F pinning mechanism discussed in this work is consistent with that observed in the MoS_2 systems.[56]

Impurities. As discussed above, the existence of impurities could dope the TMD materials and contribute to E_F pinning at a metal/TMD interface. Addou et al. have studied the concentration of such impurities for the W-TMD bulk crystals that are used in this work by ICP-MS.[61,62] We discuss the effect of these impurities on the contact performance below.

The detectable impurities of WS_2 are highlighted in the periodic table in ref 61. Te shows the highest concentration among all of the impurities. Theory calculation has predicted that Te substitution of S could lead to an increased indirect band gap for a WS_2/WSe_2 heterostructure.[68] It has been reported that Re is an n-type dopant for TMDs,[69] while Li, Na, Ca, Au, Mo, and Nb are p-type dopants.[21,64,65] Klein et al. have reported that Fe has an insignificant impact on the transport performance to W-TMD.[70] Although the concentration of all the detected elements is below the typical impurity specification ($5 \times 10^{10}/cm^2$) for Si-based technology, these impurities may dope the TMD materials and contribute to the E_F pinning after metallization, as discussed above. The impurities would also cause variation in the electronic and topographical behavior for the STM/STS characterization that will be discussed below. The discussion of the impurities detected in WSe_2 can be found elsewhere.[62] Various impurities are detected for WTe_2 as shown in ref ~~58~~. These impurities do not strongly impact the metallic property of the WTe_2 since the core level peak positions are not changed significantly as shown in Figures S2 and S4. However, these impurities may impact tribological and thermal properties of TMDs.[71,72]

Imperfections of W-TMD. Figure 5 shows the STM images obtained on a freshly exfoliated WS_2 bulk crystal surface. A WS_2 surface with dark "concave" defects is shown in Figure 5a. The STS result in Figure 5b indicates that this surface is n-type, and the band gap of the WS_2 bulk crystal is 1.49 ± 0.10 eV, which is consistent with the experimental and theoretical values.[31,73] The n-type behavior is possibly due to the sulfur deficiency which is confirmed by the W:S ratio of 1:1.86 estimated from the XPS peak fitting result. Re, a typical n-type dopant to TMDs, is detected by ICP-MS at 0.42 ppbw (2.7×10^9 atoms/cm^2) for WS_2.[58] Tang et al. have reported that oxygen can also serve as an n-type dopant for MoS_2 by *in situ* doping.[74] Although the oxidation of this WS_2 is below the detection limit of XPS as shown in Figure S5, the O dopants

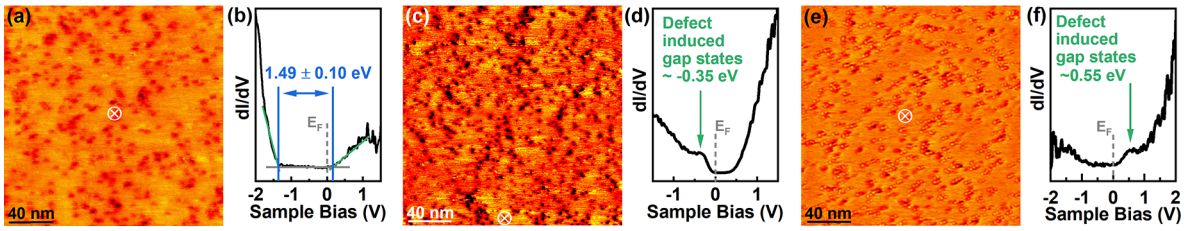

Figure 5. STM images obtained on a freshly exfoliated WS_2 bulk crystal surface at (a) 1.5 V, 0.5 nA, (c) 1 V, 0.5 nA, and (e) −0.95 V, 0.5 nA. (b), (d), and (f) are the STS taken at the white marks in (a), (c), and (e), respectively.

https://doi.org/10.1021/acsnano.3c06494
ACS Nano XXXX, XXX, XXX−XXX

could still induce n-type doping to the WS_2. Adventitious carbon is detected by XPS on the freshly exfoliated W-TMDs after the short air exposure (~1 min) in this work. This indicates that carbon species would widely exist for the devices fabricated by photolithography and polymer-assisted transfer process.[75,76] Schuler et al. have reported that C dopants substituting S sites in WS_2 would behave as charge defects and appear as depressions in the STM image.[77]

Besides the doping effect, the defects of WS_2 can also induce gap states close to the valence band and conduction band of WS_2 as shown in Figures 5d and e. Figure 5c shows an area with dark concavities and bright hillocks at a positive bias. Figure 5e shows an area with bright hillocks surrounded by dark concaves. Similar bright features are identified on MoS_2, which are attributed to metallic-like defects.[42] A bright defect, reported as a geometrically complex defect, can cause detrimental modifications in the electronic structure for WSe_2 after 600 °C annealing.[78] It is well-known that the surface of a TMD material is atomically flat in morphology by AFM. The "rough" surface obtained by STM indicates the electronic variation caused by the defects and dopants on the surface.[42,44] By changing the polarity of the imaging for the area in Figure 5e, a bright defect at a negative bias could change into a concave one at a positive bias, and a concave one at a negative bias may stay as a concave one at a positive bias as shown in Figure S7. This finding demonstrates that the defects are not topographical but rather electronic in nature, and they could behave as both donors and acceptors depending on the band bending changed with the applied bias.[79] Areas with much fewer defects are captured by STM as shown in Figure S6. This proves the spatial variation of the defect and impurity distributions across the same freshly exfoliated WS_2 surface. Besides the bias variation, the variation of the concave depth is also observed. The depth of a concave varies from 0.3 to 1.4 nm, which corresponds to 0.5 to 2.5 of the WS_2 monolayer as shown in Figure S7.

In addition to the topographical and electronic variation, atomic scale imperfections can also be found on the freshly exfoliated WS_2 surface. Figure 6b is a high magnification image around a concave defect in Figure 6a within which multiple concavities can be observed. The atomic resolution is absent in the concave depression region, highlighted by the green circle, indicating that the concave depression is probably caused by an acceptor type of defect which could deplete the electron in the vicinity of the defect. Such defects can be impurities, missing atoms, and dangling bonds.[41,80,81] Figure 6c demonstrates a defect-free atomic resolution area on WS_2. The lattice constant is measured to be 3.17 Å, which is consistent with the results characterized by X-ray diffraction.[82] Local depression (purple circle), S vacancy (white circle), and absorbate/impurity (black circle) can be seen in Figure 6e, by changing the contrast of the green rectangle area in Figure 6b. A local depression is likely due to an O substituting S (O_S) or an S vacancy (V_S) in the top and bottom sulfur layers.[77,83,84] The O_S can also contribute to the narrower band gap of the WS_2 as shown in Figure 5d, f.[74] An atomic acceptor could also contribute to the presence of a local depression.[41] Multiple localized O_S (purple circles) can be found in Figure 6f without disrupting the hexagonal structure. Surface absorbates/impurities, which behave like donors on the surface, can also be observed in Figure 6f as bright atoms highlighted by black circles. Locally excess S, S antisite, and impurities like V, Nb, Ta, Au, Cr, Mo, As, Ni, Ca, and Mg could lead to enhanced p-

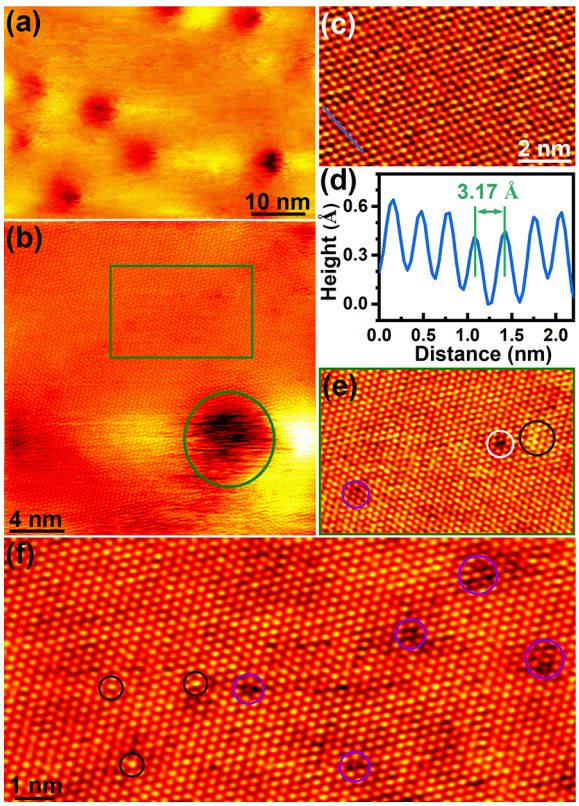

Figure 6. STM images of (a) an area with "concave" defects, (b) a high magnification image including a "concave" defect; (c) a defect-free WS_2 surface region; (d) the surface corrugation with a lattice constant of WS_2 measured to be 3.17 Å along the blue line in (c); (e) STM image showing local point defect depressions (purple), S vacancy (white), and absorbate/impurity (black); and (f) STM image presenting surface absorbates/impurities (black) and local depressions (purple). All the images are taken at −0.25 V, 1 nA.

type conductivity at a negative tip bias.[65,70,85,86] Even though the impurity concentration has been significantly minimized by using synthesized crystals instead of geological materials, the doping effect and the gap states from these defects and impurities could still considerably impact the physical and chemical properties of the TMD materials and devices.[41,44]

Reactivity. DFT calculations were performed to further understand the interface reaction between the contact metals and W-TMDs. Figure 7a−d show top views of the atomic structures of W-TMDs absorbed with single contact metal atoms. To directly quantify the strength of the interface reaction between contact metals and TMDs, we calculated the adsorption energy for metals on the surface of TMDs. For both Ni and Ag adsorption systems, their adsorption energies are negative, meaning that these systems are thermodynamically stable. For example, Ni on WSe_2 shows the lowest binding energy of −3.22 eV at the W-top site, with significantly stronger interaction with WSe_2 than that of Ag at the hollow site (−0.56 eV). A similar trend has been reported for MoS_2 systems theoretically, where single adatom adsorption of Ni on MoS_2 shows much greater binding energy than that of Ag.[87] Among the possible adsorption sites, including the W-top, chalcogen-top, and hollow site, our calculations show that Ni preferably absorbs at the W-top site, while Ag prefers the hollow site. The adsorption site preference for Ni and Ag on W-TMDs is similar to MoS_2, where Ni prefers the Mo-top site

https://doi.org/10.1021/acsnano.3c06494
ACS Nano XXXX, XXX, XXX−XXX

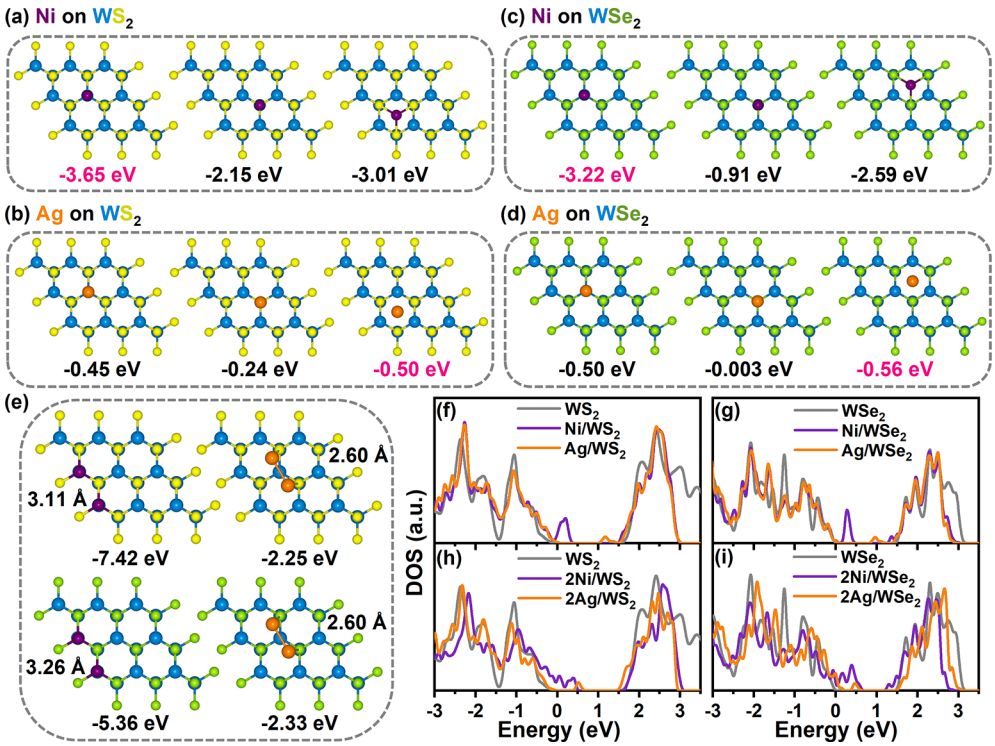

Figure 7. (a–d) Diagrams of a single metal atom adsorbed on W-TMDs with the adsorption energy listed; (e) two metal atoms adsorbed on W-TMDs with the adsorption energy and the distance of the two adatoms listed; (f–g) DOS plots of a single adatom on the W-TMDs; (h–i) DOS plots of two adatoms on the W-TMDs.

and Ag prefers the hollow site.[88] The calculated adsorption energies suggest that Ni could react with W-TMDs accompanied by a strong thermodynamic driving force (i.e., free energy gain), while Ag does not have enough driving force to react with W-TMDs. This is in good agreement with the interface chemistry results discussed above. Recently, Chen et al. have reported that Ni and Ag tend to form on-top chemisorptive and Morié physisorptive configurations with WSe_2.[46] This also agrees with our surface adsorption modeling and interface chemistry characterization results.

The density of states (DOS) has been further calculated to reveal the influence of a single surface adsorption atom on the TMD electronic structure properties. Figure 7f–g presents the DOS of WS_2 and WSe_2, with a single Ni or Ag metal adsorption. Ni induces significantly higher gap states compared to Ag, which again confirms the stronger surface reaction between Ni and W-TMDs. The above results explain the experimental observation that Ni forms covalent contacts with W-TMDs while Ag forms vdW contacts. The metal-induced gap states (MIGS), the complexity of which would increase with the number of contact metal atoms, could introduce energy levels within the band gap of TMDs.[11,89] These energy levels may serve as trapping centers for carriers and contribute to E_F pinning at a metal/TMD interface. A vdW metal, such as Ag, Bi, In, Sn, and Au, has much weaker interaction relative to a covalent metal contact, like Ni, Ti, Sc, etc., which would reduce the orbital hybridization between the metal contact and the TMD, leading to less intensive gap states.[46] Recently, Kwon et al. have reported a method of using the Se buffer layer to increase the interface gap distance between vdW Au contact and WSe_2, diminishing the overlap of the orbitals.[26] This is also in good agreement with our calculation results that a stronger interaction between a metal and a TMD could induce more intensive gap states.

The above results shed light on the Ni and Ag single adatom behaviors on W-TMDs. Experimentally, the initially deposited contact metals will form thin monolayer films or islands where metal–metal interactions could play an important role in the surface reaction. To investigate the influence of metal–metal interaction on the surface reaction, we have modeled two contact metal adatoms' adsorption behaviors on W-TMDs. Figure 7e presents the atomic structures of Ni and Ag adatoms adsorbed on W-TMDs. Like the single adatom, Ni exhibits more negative adsorption energy on WSe_2 than Ag (−5.36 vs −2.33 eV), which again suggests a stronger surface reaction between WSe_2 and Ni. Quantitatively, the adsorption energy for Ni two adatoms is less than twice (∼1.7 times) that of a single adatom, while this value for Ag two adatoms is much more than twice (∼4.2 times) that of a single adatom. This result suggests that there is a strong bonding interaction between Ag atoms, which leads to the significantly increased adsorption energy from a single Ag adatom to two Ag adatoms (from −0.56 to −2.33 eV). Namely, Ag–Ag dimer adsorption leads to a more negative binding energy. Therefore, it could be argued that during metal deposition, due to a strong Ag–Ag bonding interaction, Ag tends to form metal clusters with weak surface interactions on W-TMDs. While for Ni, there is a relatively weak Ni–Ni bonding but a strong Ni/W-TMD surface reaction. Like the single adatom systems, two Ni adatoms induce stronger gap states relative to two Ag adatoms as shown in Figure 7h–i, which confirms that Ni shows enhanced interaction with W-TMDs compared to Ag. This scenario is consistent with our experimental result that uniform Ni film forms covalent contacts, while Ag islands form vdW contacts on W-TMDs. It is worth noting that the DOS of a

https://doi.org/10.1021/acsnano.3c06494
ACS Nano XXXX, XXX, XXX–XXX

bulk metal contact/W-TMD system would show significant differences from that of the single or two adatom system due to the different number of contact metal atoms included in the calculation model.

DISCUSSION

Implications for R_c. Using the difference between the Φ of a contact metal and the electron affinity or ionization energy of a semiconductor has been considered a reliable method of predicting the SBH of the contact interface.[90−92] However, due to the complicated nature of the metal/TMD interface, significant deviation from the Schottky−Mott rule has been reported in the aspects of device performance and interface chemistry for various metal/TMD systems.[8,9,27−34] From our systematic study of the interface chemistry and band alignment of Ag/TMDs systems, the E_F pinning after Ag deposition likely originates from the doping effect by the defects and impurities of the W-TMDs. This brings up a potential strategy for tuning the R_c of TMD-based devices by intentionally doping the contact region of the TMD substrate into the bands of the semiconductors.[24,93,94] In this way, the SBH between a metal, which forms a vdW gap with TMDs, and a TMD substrate can be eliminated.

Without detectable interface reactions, the E_Fs of both WS_2 and WSe_2 after Ag deposition (Figure 4) are close to their intrinsic E_Fs before metal deposition. This fact indicates that the doping effect and the gap states from the impurities and defects captured by STM and ICP-MS examinations dominate the origin of E_F pinning for a vdW metal contact on a TMD material. Therefore, by minimizing the impurities and defects of the TMDs, it is possible to tune the band alignment by the Φ of the metal and form a vdW metal/TMD interface to follow the Schottky−Mott rule.

The formation of vdW gaps between Ag and TMDs indicates that the injection of carriers must tunnel through a barrier at the interface, which is detrimental to achieving a high on-state current. Since the reaction between Ag and TMDs is not thermodynamically favorable at room temperature, carefully raising the temperature during or postmetal deposition could promote the formation of a covalent interface and maximize the injection of the carriers. This would be a processing strategy to enhance the on-state current for a TMD-based device with vdW metal contacts, such as Ag, Pt, Pd, Au, In, Bi, and Sn.[26,34,44,45,95,96] The interface reaction products and their impact on band alignment need to be carefully characterized to optimize the carrier injection efficiency.

Recently, TMD devices using vdW contacts, such as Bi, In, Sn, Au, Ag, Co, Cu, and Pt, show significant improvement in the R_c and good agreement with the Schottky−Mott rule.[25,26,97,98] The commonality of these studies is that the damage of the TMD materials during metal contact deposition has been minimized by various methods, e.g., transferred contact, Se buffer layer, low deposition rate, and controlled radiative damage. Besides the damage during the metal deposition, the intrinsic defects of the TMDs also need to be carefully characterized and controlled to accomplish reliable and comprehensive results.[44]

Minimize Radiation Damage. To be compatible with the current industrial high-volume manufacturing process, it is vital to understand the source of damage to the TMDs during the e-beam deposition process of metal contact.[98] The thermal energy of evaporated metal atoms or clusters, the (X-ray) photons, and electron radiation from the crucible are three main sources of energetic species available to cause damage (*viz.* atomic bond scission) to the TMD samples. The formation energy of a W−Se bond is −0.872 eV,[99] and as a result, the energies to remove a Se and a W atom are 2.616 and 5.232 eV, respectively. The thermal energy of an emitted tungsten (the metal with the highest melting point) atom at its melting point (∼3030 K at 10^{-2} pa vapor pressure[100,101]) is ∼0.262 eV. This amount of energy is therefore not sufficient to break a bond of a TMD material resulting in a defect that would impact the electronic performance. Additionally, the long-throw e-beam source to sample distance and manipulator water cooling results in a sample surface temperature increase of <3 °C during the deposition in our apparatus, and thus thermal radiation from the source is also insufficient to enable bond scission, in contrast to recent reports.[98] Moreover, considering that the potential difference between the crucible and the electron source is usually in the magnitude of 10 kV,[102] the accelerated and scattered electrons are unlikely to escape from the force of the intense magnetic field (∼10^2 Gauss) around the e-beam source and the crucible. Therefore, the damage from thermal radiation, vaporized metal atoms, and stray electrons would not dominate the radiative damage to the TMD materials.

However, the energies of photons generated by Bremsstrahlung radiation of the accelerated electrons could be as high as the potential energy of the electrons (∼10 keV). Furthermore, 10 keV is enough to generate characteristic X-rays for almost all the metal elements used for contact,[103] which is consistent with the universal E_F pinning at a metal/TMD interface. This photon radiation would serve as a reasonable source of damage to the TMDs during the e-beam deposition process and is widely known as a potential source of damage in III−V device materials.[104,105] For WSe_2, the wavelength of the photon must be less than 473 nm ($h\nu$ = 2.62 eV) to create a Se vacancy. Energetic X-ray and ultraviolet (UV) photons are more likely to be the source of radiation damage during the metal deposition process. Recently, contact metals with low melting points, such as Bi, In, Sb, and Sn, demonstrate low R_c for TMD-based devices.[34,95,106] The contact metal with a low melting point would need much less power to deposit a suitable contact film, which could significantly decrease the radiation dosage of X-ray and UV light to the TMDs. The reduced dosage would thus be expected to induce fewer defects in the TMDs and relieve the E_F pinning at the contact/TMD interface. English et al. have reported that UHV deposition conditions can improve contact performance compared to HV conditions.[36] For a specific metal source, the temperature to trigger the metal vaporization decreases with the decrease of the pressure in the vacuum chamber.[107] A lower temperature requires less power applied to the metal source in the crucible. This can reduce the X-ray and UV radiation to the TMDs and hence decrease the number of defects created during the deposition process. In addition, the collision between the ∼10 keV electrons and the lightweight residual gas (such as hydrogen) could also generate energetic particles, which can transfer energy to the TMD lattice. According to the calculation by Coelho et al.,[108] this amount of energy is probably not enough to create defects, but it may develop existing defects and increase the defect density.

For a fixed acceleration voltage, the temperature of the evaporation material rises roughly linearly with the e-beam current. According to the Antoine equation in the first-order approximation, the deposition rate increases exponentially as a

https://doi.org/10.1021/acsnano.3c06494
ACS Nano XXXX, XXX, XXX−XXX

function of the e-beam current. Thus, slightly increasing the e-beam current can substantially decrease the deposition time for a target film thickness. In contrast, the X-ray intensity changes linearly with the e-beam current.[109] Therefore, the X-ray dosage would decrease drastically by increasing the deposition rate. The flux of secondary and backscattered electrons would also change linearly with the intensity of the primary electron beam, which would also minimize any potential damage to the TMDs caused by these electrons.[109] Wang et al. have reported a multistep deposition process with the formation of E_F unpinned p-type contacts on TMDs at a relatively high deposition rate (2 Å/s vs 0.1 Å/s).[98] Based on the discussion above, this intermittent e-beam deposition strategy could reduce the total X-ray dosage of the sample and decrease the damage to the TMDs. Also, the pause time between the steps could stabilize the vacuum pressure and reduce the generation of energetic residual gas particles, and hence less energy would be transferred to the surface of the sample.

Therefore, the metal deposition process, especially for the deposition rate and the vacuum condition, needs to be optimized to minimize the radiation damage, mainly from the high-energy photons, to the TMDs. The operation temperature of thermal evaporation is usually <2000 K,[110] for which the radiation is dominated by infrared and visible light. From the perspective of radiation damage, thermal evaporation might be a better solution for contact metal deposition to avoid high-energy X-ray radiation and energetic particles.

CONCLUSIONS

In this study, the origins of E_F pinning for metal contacts on W-TMDs are investigated in the aspects of interface chemistry, band alignment, impurities, imperfections, contact metal adsorption mechanism, and the resultant electronic structure. The combination of all these factors with different weights leads to various contact performances even with the same TMD and contact metal in the literature. The defects, impurities, and interface reaction product are the origins of the E_F pinning at a covalent contact metal/W-TMD interface such as Ni/W-TMDs. The electronic modification from the defects and impurities of the TMDs dominates the E_F pinning for a vdW contact metal/TMD system, e.g., Ag/W-TMDs. The MIGS would also contribute to E_F pinning for a metal/TMD interface. These results shed light on the achievement of Ohmic metal contacts on TMD materials by direct metal deposition which is compatible with the current mass manufacturing fabrication process.

EXPERIMENTAL METHODS

Metal Depositions. 2H-WS_2, 2H-WSe_2, and 1T′-WTe_2 bulk crystals (~2 mm × 2 mm), purchased from HQ Graphene,[111] were attached to a 4-in. Si wafer side by side by carbon tape. After exfoliation, the wafer was loaded into the UHV cluster tool[112] or the HV Cryo electron beam (e-beam) evaporator[113] within 1 min to minimize the contamination and oxidation of the freshly exfoliated TMD surfaces. Metal films (~1 nm Ni or Ag) were deposited at a rate of 0.1 Å/s on the freshly exfoliated TMD surfaces under UHV and HV conditions at room temperature. After metal deposition in UHV (base pressure ~3×10^{-11} mbar), the samples were *in situ* transferred through the interconnected tube under UHV conditions into the analytical chamber for interface chemistry studies. Contamination should be minimized by employing the UHV *in situ* process. Therefore, intrinsic interface reactions can be obtained for the metal/W-TMD interfaces deposited under UHV conditions. After metal deposition in HV (base pressure ~3×10^{-6} mbar), the samples were transferred *ex situ* into the cluster tool for interface chemistry characterization. The air exposure of the samples was ~5 min during the *ex situ* transfer process. Identical deposition and transfer procedures were employed as reported in previous work.[56] Ni and Ag reference spectra were obtained from the *in situ* (~30 nm) metal films also deposited under UHV conditions. The oxidation of the reference metal films was below the detection limit of XPS. Their carbon contamination is close to the detection limit of XPS.

XPS. The core level spectra were collected at a takeoff angle of 45° using a monochromatic Al Kα_1 X-ray source and an Omicron EA 125 hemispherical analyzer. The pass energy for core level scans was 15 eV under the constant analysis energy mode with an energy resolution of 0.05 eV. The energy analyzer was calibrated following the ASTM E2108 standard procedure employing sputter-cleaned Au, Ag, and Cu foils.[114] The scan spot size is ~1.5 mm with ±8° angular acceptance. (This spot size is very close to the size of the TMD crystals. Therefore, it is reasonable to consider that most of the adventitious carbon signal (~20 atomic%) is from the exposed carbon tape.) The core level peaks were fitted using the AAnalyzer peak fitting software.[115] Consistent fitting parameters (peak width, background type, doublet separations) were utilized for the same core level spectra. The fitting residual of each core level spectrum was within the noise level.

AFM. Veeco model 3100 Dimension V and Oxford Asylum Research Jupiter XF AFM instruments were employed in tapping mode to acquire the surface morphology of the TMD surfaces after metal deposition. The RMS roughness of the AFM images was calculated by the WSxM software.[116]

STM/STS. The STM images were acquired using an Omicron VT-AFM system with constant current mode at room temperature. Each STS spectrum is averaged from at least 17 repetitions to enhance the signal-to-noise ratio. The STM images were processed using Gwyddion software.[117]

DFT Calculations. DFT calculations were performed by using the Vienna Ab initio Simulation Package (VASP)[118,119] with projected augmented wave (PAW)[120,121] pseudopotentials. The Perdew−Burke−Ernzerhof generalized gradient approximation (GGA-PBE) functional[122,123] was employed to describe the exchange-correlation potential energy between electrons. A cutoff energy of 520 eV was used. The Monkhorst−Pack scheme with a 5 × 5 × 1 mesh was used for Brillouin-zone *k*-point sampling. The conjugated gradient method was used for structural optimization with the convergence criterion of the force on each atom less than 0.01 eV/Å. Electronic minimization was performed by using a blocked Davidson iteration scheme until total system energy converges at 10^{-5} eV. For the interface reaction modeling, the metal-adsorbed TMD systems were constructed by placing the contact metal atoms on top of four TMD layers. A 15-Å-thick vacuum layer along the *z*-direction was introduced to the surface adsorption slab model to decouple the adjacent periodic images. The adsorption energy was calculated according to $E_{ad} = E_{(M/TMD)} - E_{(TMD)} - E_{(M)}$ where $E_{(M/TMD)}$ is the energy of the metal adsorbed TMD, and $E_{(TMD)}$ and $E_{(M)}$ are the energies of the isolated TMD and metal atom(s) before adsorption, respectively.

ASSOCIATED CONTENT

Supporting Information

The Supporting Information is available free of charge at https://pubs.acs.org/doi/10.1021/acsnano.3c06494.

Interface chemistry and surface morphology of Ni/WSe_2, Ni/WTe_2, Ag/WS_2, and Ag/WTe_2; The fwhm's of the TMD bulk crystal and Ag metal chemical states before and after Ag depositions; The binding energies of W-TMD states in W $4f_{7/2}$, S $2p_{3/2}$, and Se $3d_{5/2}$ spectra; ICP-MS results of W-TMDs; XPS spectra of the freshly exfoliated WS_2 for STM/STS; Freshly exfoliated WS_2 surface with fewer defects; Bias-dependent electronic variation and the depth variation of the ~~concaves~~ on the

https://doi.org/10.1021/acsnano.3c06494
ACS Nano XXXX, XXX, XXX−XXX

fresh exfoliated WS_2 surface. The extraction of the band alignment by XPS. (PDF)

AUTHOR INFORMATION

Corresponding Author

Robert M. Wallace − *Department of Materials Science and Engineering, The University of Texas at Dallas, Richardson, Texas 75080, United States;* orcid.org/0000-0001-5566-4806; Email: rmwallace@utdallas.edu

Authors

Xinglu Wang − *Department of Materials Science and Engineering, The University of Texas at Dallas, Richardson, Texas 75080, United States;* orcid.org/0000-0003-2466-6889

Yaoqiao Hu − *Department of Materials Science and Engineering, The University of Texas at Dallas, Richardson, Texas 75080, United States;* orcid.org/0000-0002-0701-1613

Seong Yeoul Kim − *Department of Materials Science and Engineering, The University of Texas at Dallas, Richardson, Texas 75080, United States*

Rafik Addou − *Department of Materials Science and Engineering, The University of Texas at Dallas, Richardson, Texas 75080, United States;* orcid.org/0000-0002-5454-0315

Kyeongjae Cho − *Department of Materials Science and Engineering, The University of Texas at Dallas, Richardson, Texas 75080, United States;* orcid.org/0000-0003-2698-7774

Complete contact information is available at: https://pubs.acs.org/10.1021/acsnano.3c06494

Notes

The authors declare no competing financial interest.

ACKNOWLEDGMENTS

This work was supported in part by NEWLIMITS, a center in nCORE, a Semiconductor Research Corporation (SRC) program sponsored by NIST through award number 70NANB17H041, and by the National Science Foundation through award DMR-2002741.

REFERENCES

(1) Radisavljevic, B.; Radenovic, A.; Brivio, J.; Giacometti, V.; Kis, A. Single-Layer MoS_2 Transistors. *Nat. Nanotechnol.* **2011**, *6*, 147−150.

(2) Splendiani, A.; Sun, L.; Zhang, Y.; Li, T.; Kim, J.; Chim, C.-Y.; Galli, G.; Wang, F. Emerging Photoluminescence in Monolayer MoS_2. *Nano Lett.* **2010**, *10*, 1271−1275.

(3) Akinwande, D.; Petrone, N.; Hone, J. Two-Dimensional Flexible Nanoelectronics. *Nat. Commun.* **2014**, *5*, 5678.

(4) Soluyanov, A. A.; Gresch, D.; Wang, Z.; Wu, Q.; Troyer, M.; Dai, X.; Bernevig, B. A. Type-II Weyl Semimetals. *Nature* **2015**, *527*, 495−498.

(5) Zhu, Z. Y.; Cheng, Y. C.; Schwingenschlögl, U. Giant Spin-Orbit-Induced Spin Splitting in Two-Dimensional Transition-Metal Dichalcogenide Semiconductors. *Phys. Rev. B* **2011**, *84*, 153402.

(6) Ng, H. K.; Xiang, D.; Suwardi, A.; Hu, G.; Yang, K.; Zhao, Y.; Liu, T.; Cao, Z.; Liu, H.; Li, S.; Cao, J.; Zhu, Q.; Dong, Z.; Tan, C. K. I.; Chi, D.; Qiu, C.-W.; Hippalgaonkar, K.; Eda, G.; Yang, M.; Wu, J. Improving Carrier Mobility in Two-Dimensional Semiconductors with Rippled Materials. *Nat. Electron.* **2022**, *5*, 489−496.

(7) Wu, R.; Tao, Q.; Li, J.; Li, W.; Chen, Y.; Lu, Z.; Shu, Z.; Zhao, B.; Ma, H.; Zhang, Z.; Yang, X.; Li, B.; Duan, H.; Liao, L.; Liu, Y.; Duan, X.; Duan, X. Bilayer Tungsten Diselenide Transistors with On-State Currents Exceeding 1.5 Milliamperes Per Micrometre. *Nat. Electron.* **2022**, *5*, 497−504.

(8) Das, S.; Chen, H.-Y.; Penumatcha, A. V.; Appenzeller, J. High Performance Multilayer MoS_2 Transistors with Scandium Contacts. *Nano Lett.* **2013**, *13*, 100−105.

(9) Kim, G.-S.; Kim, S.-H.; Park, J.; Han, K. H.; Kim, J.; Yu, H.-Y. Schottky Barrier Height Engineering for Electrical Contacts of Multilayered MoS_2 Transistors with Reduction of Metal-Induced Gap States. *ACS Nano* **2018**, *12*, 6292−6300.

(10) Fang, H.; Chuang, S.; Chang, T. C.; Takei, K.; Takahashi, T.; Javey, A. High-Performance Single Layered WSe_2 P-FETs with Chemically Doped Contacts. *Nano Lett.* **2012**, *12*, 3788−3792.

(11) Gong, C.; Colombo, L.; Wallace, R. M.; Cho, K. The Unusual Mechanism of Partial Fermi Level Pinning at Metal-MoS_2 Interfaces. *Nano Lett.* **2014**, *14*, 1714−1720.

(12) Andrews, K.; Bowman, A.; Rijal, U.; Chen, P.-Y.; Zhou, Z. Improved Contacts and Device Performance in MoS_2 Transistors Using a 2D Semiconductor Interlayer. *ACS Nano* **2020**, *14*, 6232−6241.

(13) Du, Y.; Yang, L.; Zhang, J.; Liu, H.; Majumdar, K.; Kirsch, P. D.; Ye, P. D. MoS_2 Field-Effect Transistors with Graphene/Metal Heterocontacts. *IEEE Electron Device Lett.* **2014**, *35*, 599−601.

(14) Das, S.; Gulotty, R.; Sumant, A. V.; Roelofs, A. All Two-Dimensional, Flexible, Transparent, and Thinnest Thin Film Transistor. *Nano Lett.* **2014**, *14*, 2861−2866.

(15) Roy, T.; Tosun, M.; Kang, J. S.; Sachid, A. B.; Desai, S. B.; Hettick, M.; Hu, C. C.; Javey, A. Field-Effect Transistors Built from All Two-Dimensional Material Components. *ACS Nano* **2014**, *8*, 6259−6264.

(16) McDonnell, S.; Azcatl, A.; Addou, R.; Gong, C.; Battaglia, C.; Chuang, S.; Cho, K.; Javey, A.; Wallace, R. M. Hole Contacts on Transition Metal Dichalcogenides: Interface Chemistry and Band Alignments. *ACS Nano* **2014**, *8*, 6265−6272.

(17) Wang, J.; Yao, Q.; Huang, C.-W.; Zou, X.; Liao, L.; Chen, S.; Fan, Z.; Zhang, K.; Wu, W.; Xiao, X.; Jiang, C.; Wu, W.-W. High Mobility MoS_2 Transistor with Low Schottky Barrier Contact by Using Atomic Thick h-BN as a Tunneling Layer. *Adv. Mater.* **2016**, *28*, 8302−8308.

(18) Xie, L.; Liao, M.; Wang, S.; Yu, H.; Du, L.; Tang, J.; Zhao, J.; Zhang, J.; Chen, P.; Lu, X.; Wang, G.; Xie, G.; Yang, R.; Shi, D.; Zhang, G. Graphene-Contacted Ultrashort Channel Monolayer MoS_2 Transistors. *Adv. Mater.* **2017**, *29*, 1702522.

(19) Kappera, R.; Voiry, D.; Yalcin, S. E.; Branch, B.; Gupta, G.; Mohite, A. D.; Chhowalla, M. Phase-Engineered Low-Resistance Contacts for Ultrathin MoS_2 Transistors. *Nat. Mater.* **2014**, *13*, 1128−1134.

(20) Cho, S.; Kim, S.; Kim, J. H.; Zhao, J.; Seok, J.; Keum, D. H.; Baik, J.; Choe, D.-H.; Chang, K. J.; Suenaga, K.; Kim, S. W.; Lee, Y. H.; Yang, H. Phase Patterning for Ohmic Homojunction Contact in $MoTe_2$. *Science* **2015**, *349*, 625.

(21) Fang, H.; Tosun, M.; Seol, G.; Chang, T. C.; Takei, K.; Guo, J.; Javey, A. Degenerate N-Doping of Few-Layer Transition Metal Dichalcogenides by Potassium. *Nano Lett.* **2013**, *13*, 1991−1995.

(22) Suh, J.; Park, T.-E.; Lin, D.-Y.; Fu, D.; Park, J.; Jung, H. J.; Chen, Y.; Ko, C.; Jang, C.; Sun, Y.; Sinclair, R.; Chang, J.; Tongay, S.; Wu, J. Doping against the Native Propensity of MoS_2: Degenerate Hole Doping by Cation Substitution. *Nano Lett.* **2014**, *14*, 6976−6982.

(23) Kiriya, D.; Tosun, M.; Zhao, P.; Kang, J. S.; Javey, A. Air-Stable Surface Charge Transfer Doping of MoS_2 by Benzyl Viologen. *J. Am. Chem. Soc.* **2014**, *136*, 7853−7856.

(24) Yang, L.; Majumdar, K.; Liu, H.; Du, Y.; Wu, H.; Hatzistergos, M.; Hung, P. Y.; Tieckelmann, R.; Tsai, W.; Hobbs, C.; Ye, P. D. Chloride Molecular Doping Technique on 2D Materials: WS_2 and MoS_2. *Nano Lett.* **2014**, *14*, 6275−6280.

(25) Liu, Y.; Guo, J.; Zhu, E.; Liao, L.; Lee, S.-J.; Ding, M.; Shakir, I.; Gambin, V.; Huang, Y.; Duan, X. Approaching the Schottky-Mott

Limit in van der Waals Metal-Semiconductor Junctions. *Nature* **2018**, *557*, 696−700.

(26) Kwon, G.; Choi, Y.-H.; Lee, H.; Kim, H.-S.; Jeong, J.; Jeong, K.; Baik, M.; Kwon, H.; Ahn, J.; Lee, E.; Cho, M.-H. Interaction- and Defect-Free van der Waals Contacts between Metals and Two-Dimensional Semiconductors. *Nat. Electron.* **2022**, *5*, 241−247.

(27) Schauble, K.; Zakhidov, D.; Yalon, E.; Deshmukh, S.; Grady, R. W.; Cooley, K. A.; McClellan, C. J.; Vaziri, S.; Passarello, D.; Mohney, S. E.; Toney, M. F.; Sood, A. K.; Salleo, A.; Pop, E. Uncovering the Effects of Metal Contacts on Monolayer MoS_2. *ACS Nano* **2020**, *14*, 14798−14808.

(28) Kim, C.; Moon, I.; Lee, D.; Choi, M. S.; Ahmed, F.; Nam, S.; Cho, Y.; Shin, H.-J.; Park, S.; Yoo, W. J. Fermi Level Pinning at Electrical Metal Contacts of Monolayer Molybdenum Dichalcogenides. *ACS Nano* **2017**, *11*, 1588−1596.

(29) Liu, W.; Kang, J.; Sarkar, D.; Khatami, Y.; Jena, D.; Banerjee, K. Role of Metal Contacts in Designing High-Performance Monolayer N-Type WSe_2 Field Effect Transistors. *Nano Lett.* **2013**, *13*, 1983−1990.

(30) Smyth, C. M.; Addou, R.; McDonnell, S.; Hinkle, C. L.; Wallace, R. M. WSe_2-Contact Metal Interface Chemistry and Band Alignment under High Vacuum and Ultra High Vacuum Deposition Conditions. *2D Mater.* **2017**, *4*, 025084.

(31) Smyth, C. M.; Addou, R.; Hinkle, C. L.; Wallace, R. M. Origins of Fermi Level Pinning between Tungsten Dichalcogenides (WS_2, WTe_2) and Bulk Metal Contacts: Interface Chemistry and Band Alignment. *J. Phys. Chem. C* **2020**, *124*, 14550−14563.

(32) Kang, J.; Liu, W.; Banerjee, K. High-Performance MoS_2 Transistors with Low-Resistance Molybdenum Contacts. *Appl. Phys. Lett.* **2014**, *104*, 093106.

(33) Chou, A. S.; Cheng, C. C.; Liew, S. L.; Ho, P. H.; Wang, S. Y.; Chang, Y. C.; Chang, C. K.; Su, Y. C.; Huang, Z. D.; Fu, F. Y.; Hsu, C. F.; Chung, Y. Y.; Chang, W. H.; Li, L. J.; Wu, C. I. High On-State Current in Chemical Vapor Deposited Monolayer MoS_2 NFETs with Sn Ohmic Contacts. *IEEE Electron Device Lett.* **2021**, *42*, 272.

(34) Wang, Y.; Kim, J. C.; Wu, R. J.; Martinez, J.; Song, X.; Yang, J.; Zhao, F.; Mkhoyan, A.; Jeong, H. Y.; Chhowalla, M. van der Waals Contacts between Three-Dimensional Metals and Two-Dimensional Semiconductors. *Nature* **2019**, *568*, 70−74.

(35) O'Brien, K. P.; Dorow, C. J.; Penumatcha, A.; Maxey, K.; Lee, S.; Naylor, C. H.; Hsiao, A.; Holybee, B.; Rogan, C.; Adams, D.; Tronic, T.; Ma, S.; Oni, A.; Gupta, A. S.; Bristol, R.; Clendenning, S.; Metz, M.; Avci, U., Advancing 2D Monolayer CMOS through Contact, Channel and Interface Engineering. In *2021 IEEE International Electron Devices Meeting (IEDM)*; IEEE: **2021**; pp 7.1.1−7.1.4.

(36) English, C. D.; Shine, G.; Dorgan, V. E.; Saraswat, K. C.; Pop, E. Improved Contacts to MoS_2 Transistors by Ultra-High Vacuum Metal Deposition. *Nano Lett.* **2016**, *16*, 3824−3830.

(37) Smyth, C. M.; Walsh, L. A.; Bolshakov, P.; Catalano, M.; Schmidt, M.; Sheehan, B.; Addou, R.; Wang, L.; Kim, J.; Kim, M. J.; Young, C. D.; Hinkle, C. L.; Wallace, R. M. Engineering the Interface Chemistry for Scandium Electron Contacts in WSe_2 Transistors and Diodes. *2D Mater.* **2019**, *6*, 045020.

(38) McDonnell, S.; Smyth, C.; Hinkle, C. L.; Wallace, R. M. MoS_2-Titanium Contact Interface Reactions. *ACS Appl. Mater. Interfaces* **2016**, *8*, 8289−8294.

(39) Leonhardt, A.; Chiappe, D.; Asselberghs, I.; Huyghebaert, C.; Radu, I.; De Gendt, S. Improving MOCVD MoS_2 Electrical Performance: Impact of Minimized Water and Air Exposure Conditions. *IEEE Electron Device Lett.* **2017**, *38*, 1606−1609.

(40) Mondal, A.; Biswas, C.; Park, S.; Cha, W.; Kang, S.-H.; Yoon, M.; Choi, S. H.; Kim, K. K.; Lee, Y. H. Low Ohmic Contact Resistance and High on/off Ratio in Transition Metal Dichalcogenides Field-Effect Transistors via Residue-Free Transfer. *Nat. Nanotechnol.* **2023**, DOI: 10.1038/s41565-023-01497-x.

(41) Addou, R.; McDonnell, S.; Barrera, D.; Guo, Z.; Azcatl, A.; Wang, J.; Zhu, H.; Hinkle, C. L.; Quevedo-Lopez, M.; Alshareef, H. N.; Colombo, L.; Hsu, J. W. P.; Wallace, R. M. Impurities and Electronic Property Variations of Natural MoS_2 Crystal Surfaces. *ACS Nano* **2015**, *9*, 9124−9133.

(42) Addou, R.; Colombo, L.; Wallace, R. M. Surface Defects on Natural MoS_2. *ACS Appl. Mater. Interfaces* **2015**, *7*, 11921−11929.

(43) Jeong, T. Y.; Kim, H.; Choi, S.-J.; Watanabe, K.; Taniguchi, T.; Yee, K. J.; Kim, Y.-S.; Jung, S. Spectroscopic Studies of Atomic Defects and Bandgap Renormalization in Semiconducting Monolayer Transition Metal Dichalcogenides. *Nat. Commun.* **2019**, *10*, 3825.

(44) McDonnell, S.; Addou, R.; Buie, C.; Wallace, R. M.; Hinkle, C. L. Defect-Dominated Doping and Contact Resistance in MoS_2. *ACS Nano* **2014**, *8*, 2880−2888.

(45) Smyth, C. M.; Addou, R.; McDonnell, S.; Hinkle, C. L.; Wallace, R. M. Contact Metal-MoS_2 Interfacial Reactions and Potential Implications on MoS_2-Based Device Performance. *J. Phys. Chem. C* **2016**, *120*, 14719−14729.

(46) Chen, J.; Zhang, Z.; Guo, Y.; Robertson, J. Metal Contacts with Moire Interfaces on WSe_2 for Ambipolar Applications. *Appl. Phys. Lett.* **2022**, *121*, 051602.

(47) Zhang, Z.; Guo, Y.; Robertson, J. Reduced Fermi Level Pinning at Physisorptive Sites of Moire-MoS_2 Metal Schottky Barriers. *ACS Appl. Mater. Interfaces* **2022**, *14*, 11903−11909.

(48) McClellan, C. J.; Suryavanshi, S. V.; English, C. D.; Smithe, K. K. H.; Bailey, C. S.; Grady, R. W.; Pop, E. 2d Device Trends. http://2d.stanford.edu (accessed September 13).

(49) Li, W.; Zhou, J.; Cai, S.; Yu, Z.; Zhang, J.; Fang, N.; Li, T.; Wu, Y.; Chen, T.; Xie, X.; Ma, H.; Yan, K.; Dai, N.; Wu, X.; Zhao, H.; Wang, Z.; He, D.; Pan, L.; Shi, Y.; Wang, P.; Chen, W.; Nagashio, K.; Duan, X.; Wang, X. Uniform and Ultrathin High-k Gate Dielectrics for Two-Dimensional Electronic Devices. *Nat. Electron.* **2019**, *2*, 563−571.

(50) Pang, C.; Hung, T. Y. T.; Khosravi, A.; Addou, R.; Wallace, R. M.; Chen, Z. Doping-Induced Schottky-Barrier Realignment for Unipolar and High Hole Current WSe_2 Devices with > 10^8 on/off Ratio. *IEEE Electron Device Lett.* **2020**, *41*, 1122−1125.

(51) Ovchinnikov, D.; Allain, A.; Huang, Y.-S.; Dumcenco, D.; Kis, A. Electrical Transport Properties of Single-Layer WS_2. *ACS Nano* **2014**, *8*, 8174−8181.

(52) Yeh, C.-H.; Chen, H.-C.; Lin, H.-C.; Lin, Y.-C.; Liang, Z.-Y.; Chou, M.-Y.; Suenaga, K.; Chiu, P.-W. Ultrafast Monolayer In/Gr-WS_2-Gr Hybrid Photodetectors with High Gain. *ACS Nano* **2019**, *13*, 3269−3279.

(53) Sung, J. H.; Heo, H.; Si, S.; Kim, Y. H.; Noh, H. R.; Song, K.; Kim, J.; Lee, C.-S.; Seo, S.-Y.; Kim, D.-H.; Kim, H. K.; Yeom, H. W.; Kim, T.-H.; Choi, S.-Y.; Kim, J. S.; Jo, M.-H. Coplanar Semiconductor-Metal Circuitry Defined on Few-Layer $MoTe_2$ via Polymorphic Heteroepitaxy. *Nat. Nanotechnol.* **2017**, *12*, 1064−1070.

(54) Mleczko, M. J.; Xu, R. L.; Okabe, K.; Kuo, H.-H.; Fisher, I. R.; Wong, H. S. P.; Nishi, Y.; Pop, E. High Current Density and Low Thermal Conductivity of Atomically Thin Semimetallic WTe_2. *ACS Nano* **2016**, *10*, 7507−7514.

(55) Rai, A.; Valsaraj, A.; Movva, H. C. P.; Roy, A.; Ghosh, R.; Sonde, S.; Kang, S.; Chang, J.; Trivedi, T.; Dey, R.; Guchhait, S.; Larentis, S.; Register, L. F.; Tutuc, E.; Banerjee, S. K. Air Stable Doping and Intrinsic Mobility Enhancement in Monolayer Molybdenum Disulfide by Amorphous Titanium Suboxide Encapsulation. *Nano Lett.* **2015**, *15*, 4329−4336.

(56) Wang, X.; Kim, S. Y.; Wallace, R. M. Interface Chemistry and Band Alignment Study of Ni and Ag Contacts on MoS_2. *ACS Appl. Mater. Interfaces* **2021**, *13*, 15802−15810.

(57) Wood, D. M. Classical Size Dependence of the Work Function of Small Metallic Spheres. *Phys. Rev. Lett.* **1981**, *46*, 749−749.

(58) Fadley, C. S.; Shirley, D. A. Electronic Densities of States from X-Ray Photoelectron Spectroscopy. *J. Res. Natl. Bur Stand A Phys. Chem.* **1970**, *74A*, 543−558.

(59) Smyth, C. M.; Walsh, L. A.; Bolshakov, P.; Catalano, M.; Addou, R.; Wang, L.; Kim, J.; Kim, M. J.; Young, C. D.; Hinkle, C. L.; Wallace, R. M. Engineering the Palladium-WSe_2 Interface Chemistry for Field Effect Transistors with High-Performance Hole Contacts. *ACS Appl. Nano Mater.* **2019**, *2*, 75−88.

https://doi.org/10.1021/acsnano.3c06494
ACS Nano XXXX, XXX, XXX−XXX

(60) Smyth, C. M.; Addou, R.; Hinkle, C. L.; Wallace, R. M. Origins of Fermi-Level Pinning between Molybdenum Dichalcogenides ($MoSe_2$, $MoTe_2$) and Bulk Metal Contacts: Interface Chemistry and Band Alignment. *J. Phys. Chem. C* **2019**, *123*, 23919−23930.

(61) Addou, R.; Wallace, R. M. Integration of 2D Materials for Advanced Devices: Challenges and Opportunities. *ECS Trans.* **2017**, *79*, 11−20.

(62) Addou, R.; Wallace, R. M. Surface Analysis of WSe_2 Crystals: Spatial and Electronic Variability. *ACS Appl. Mater. Interfaces* **2016**, *8*, 26400−26406.

(63) Han, D.; Ming, W.; Xu, H.; Chen, S.; Sun, D.; Du, M.-H. Chemical Trend of Transition-Metal Doping in WSe_2. *Phys. Rev. Appl.* **2019**, *12*, 034038.

(64) Schellenberger, A.; Schlaf, R.; Pettenkofer, C.; Jaegermann, W. Synchrotron-Induced Surface-Photovoltage Saturation at Intercalated Na/WSe_2 Interfaces. *Phys. Rev. B* **1992**, *45*, 3538−3545.

(65) Li, H.; Liu, S.; Huang, S.; Zhang, Q.; Li, C.; Liu, X.; Meng, J.; Tian, Y. Metallic Impurities Induced Electronic Transport in WSe_2: First-Principle Calculations. *Chem. Phys. Lett.* **2016**, *658*, 83−87.

(66) Deshpande, M.; Patel, P.; Vashi, M.; Agarwal, M. Effect of Intercalating Indium in WSe_2 Single Crystals. *J. Cryst. Growth* **1999**, *197*, 833−840.

(67) Stolz, S.; Kozhakhmetov, A.; Dong, C.; Gröning, O.; Robinson, J. A.; Schuler, B. Layer-Dependent Schottky Contact at van der Waals Interfaces: V-Doped WSe_2 on Graphene. *npj 2D Mater. Appl.* **2022**, *6*, 66.

(68) Krivosheeva, A.; Shaposhnikov, V.; Borisenko, V.; Lazzari, J.-L. Energy Band Gap Tuning in Te-Doped WS_2/WSe_2 Heterostructures. *J. Mater. Sci.* **2020**, *55*, 9695−9702.

(69) Zhang, K.; Bersch, B. M.; Joshi, J.; Addou, R.; Cormier, C. R.; Zhang, C.; Xu, K.; Briggs, N. C.; Wang, K.; Subramanian, S.; Cho, K.; Fullerton-Shirey, S.; Wallace, R. M.; Vora, P. M.; Robinson, J. A. Tuning the Electronic and Photonic Properties of Monolayer MoS_2 via In situ Rhenium Substitutional Doping. *Adv. Funct. Mater.* **2018**, *28*, 1706950.

(70) Klein, A.; Dolatzoglou, P.; Lux-Steiner, M.; Bucher, E. Influence of Material Synthesis and Doping on the Transport Properties of WSe_2 Single Crystals Grown by Selenium Transport. *Sol. Energy Mater. Sol. Cells* **1997**, *46*, 175−186.

(71) Li, W.; Hu, L.; Wang, M.; Tang, H.; Li, C.; Liang, J.; Jin, Y.; Li, D. Synthesis and Tribological Properties of Mo-Doped WSe_2 Nanolamellars. *Cryst. Res. Technol.* **2012**, *47*, 876−881.

(72) Kriener, M.; Kikkawa, A.; Suzuki, T.; Akashi, R.; Arita, R.; Tokura, Y.; Taguchi, Y. Modification of Electronic Structure and Thermoelectric Properties of Hole-Doped Tungsten Dichalcogenides. *Phys. Rev. B* **2015**, *91*, 075205.

(73) Guo, Y.; Robertson, J. Band Engineering in Transition Metal Dichalcogenides: Stacked Versus Lateral Heterostructures. *Appl. Phys. Lett.* **2016**, *108*, 233104.

(74) Tang, J.; Wei, Z.; Wang, Q.; Wang, Y.; Han, B.; Li, X.; Huang, B.; Liao, M.; Liu, J.; Li, N.; Zhao, Y.; Shen, C.; Guo, Y.; Bai, X.; Gao, P.; Yang, W.; Chen, L.; Wu, K.; Yang, R.; Shi, D.; Zhang, G. In situ Oxygen Doping of Monolayer MoS_2 for Novel Electronics. *Small* **2020**, *16*, 2004276.

(75) Liang, J.; Xu, K.; Toncini, B.; Bersch, B.; Jariwala, B.; Lin, Y. C.; Robinson, J.; Fullerton-Shirey, S. K. Impact of Post-Lithography Polymer Residue on the Electrical Characteristics of MoS_2 and WSe_2 Field Effect Transistors. *Adv. Mater. Interfaces* **2019**, *6*, 1801321.

(76) Bolshakov, P.; Smyth, C. M.; Khosravi, A.; Zhao, P.; Hurley, P. K.; Hinkle, C. L.; Wallace, R. M.; Young, C. D. Contact Engineering for Dual-Gate MoS_2 Transistors Using O_2 Plasma Exposure. *ACS Appl. Electron. Mater.* **2019**, *1*, 210−219.

(77) Schuler, B.; Lee, J.-H.; Kastl, C.; Cochrane, K. A.; Chen, C. T.; Refaely-Abramson, S.; Yuan, S.; Van Veen, E.; Roldán, R.; Borys, N. J.; Koch, R. J.; Aloni, S.; Schwartzberg, A. M.; Ogletree, D. F.; Neaton, J. B.; Weber-Bargioni, A. How Substitutional Point Defects in Two-Dimensional WS_2 Induce Charge Localization, Spin-Orbit Splitting, and Strain. *ACS Nano* **2019**, *13*, 10520−10534.

(78) Blades, W. H.; Frady, N. J.; Litwin, P. M.; Mcdonnell, S. J.; Reinke, P. Thermally Induced Defects on WSe_2. *J. Phys. Chem. C* **2020**, *124*, 15337−15346.

(79) Leon, C. C.; Kuhnke, K.; Gunnarsson, O. Band Bending and Beyond. *J. Phys. Chem. C* **2021**, *125*, 3206−3214.

(80) Ma, N.; Jena, D. Charge Scattering and Mobility in Atomically Thin Semiconductors. *Phys. Rev. X.* **2014**, *4*, 011043.

(81) KC, S.; Longo, R. C.; Addou, R.; Wallace, R. M.; Cho, K. Impact of Intrinsic Atomic Defects on the Electronic Structure of MoS_2 Monolayers. *Nanotechnology* **2014**, *25*, 375703.

(82) Wildervanck, J. C.; Jellinek, F. Preparation and Crystallinity of Molybdenum and Tungsten Sulfides. *Z. Anorg. Allg. Chem.* **1964**, *328*, 309−318.

(83) Zhu, H.; Wang, Q.; Cheng, L.; Addou, R.; Kim, J.; Kim, M. J.; Wallace, R. M. Defects and Surface Structural Stability of $MoTe_2$ under Vacuum Annealing. *ACS Nano* **2017**, *11*, 11005−11014.

(84) Schuler, B.; Qiu, D. Y.; Refaely-Abramson, S.; Kastl, C.; Chen, C. T.; Barja, S.; Koch, R. J.; Ogletree, D. F.; Aloni, S.; Schwartzberg, A. M.; Neaton, J. B.; Louie, S. G.; Weber-Bargioni, A. Large Spin-Orbit Splitting of Deep in-Gap Defect States of Engineered Sulfur Vacancies in Monolayer WS_2. *Phys. Rev. Lett.* **2019**, *123*, 076801.

(85) Edelberg, D.; Rhodes, D.; Kerelsky, A.; Kim, B.; Wang, J.; Zangiabadi, A.; Kim, C.; Abhinandan, A.; Ardelean, J.; Scully, M.; Scullion, D.; Embon, L.; Zu, R.; Santos, E. J. G.; Balicas, L.; Marianetti, C.; Barmak, K.; Zhu, X.; Hone, J.; Pasupathy, A. N. Approaching the Intrinsic Limit in Transition Metal Diselenides via Point Defect Control. *Nano Lett.* **2019**, *19*, 4371−4379.

(86) Zheng, H.; Choi, Y.; Baniasadi, F.; Hu, D.; Jiao, L.; Park, K.; Tao, C. Visualization of Point Defects in Ultrathin Layered 1T-$PtSe_2$. *2D Mater.* **2019**, *6*, 041005.

(87) Rastogi, P.; Kumar, S.; Bhowmick, S.; Agarwal, A.; Chauhan, Y. S. Doping Strategies for Monolayer MoS_2 via Surface Adsorption: A Systematic Study. *J. Phys. Chem. C* **2014**, *118*, 30309−30314.

(88) Costa-Amaral, R.; Forhat, A.; Caturello, N. A. M. S.; Silva, J. L. F. D. Unveiling the Adsorption Properties of 3d, 4d, and 5d Metal Adatoms on the MoS_2 Monolayer: A DFT-D3 Investigation. *Surf. Sci.* **2020**, *701*, 121700.

(89) Gong, C.; Huang, C.; Miller, J.; Cheng, L.; Hao, Y.; Cobden, D.; Kim, J.; Ruoff, R. S.; Wallace, R. M.; Cho, K.; Xu, X.; Chabal, Y. J. Metal Contacts on Physical Vapor Deposited Monolayer MoS_2. *ACS Nano* **2013**, *7*, 11350−11357.

(90) Brillson, L. J. Transition in Schottky Barrier Formation with Chemical Reactivity. *Phys. Rev. Lett.* **1978**, *40*, 260−263.

(91) Ayers, P. W.; Anderson, J. S. M.; Bartolotti, L. J. Perturbative Perspectives on the Chemical Reaction Prediction Problem. *Int. J. Quantum Chem.* **2005**, *101*, 520−534.

(92) King, S. W.; French, M.; Jaehnig, M.; Kuhn, M.; Boyanov, B.; French, B. X-Ray Photoelectron Spectroscopy Measurement of the Schottky Barrier at the SiC(N)/Cu Interface. *J. Vac. Sci. Technol. B* **2011**, *29*, 051207.

(93) Azcatl, A.; Qin, X.; Prakash, A.; Zhang, C.; Cheng, L.; Wang, Q.; Lu, N.; Kim, M. J.; Kim, J.; Cho, K.; Addou, R.; Hinkle, C. L.; Appenzeller, J.; Wallace, R. M. Covalent Nitrogen Doping and Compressive Strain in MoS_2 by Remote N_2 Plasma Exposure. *Nano Lett.* **2016**, *16*, 5437−5443.

(94) Pang, C.-S.; Hung, T. Y. T.; Khosravi, A.; Addou, R.; Wang, Q.; Kim, M. J.; Wallace, R. M.; Chen, Z. Atomically Controlled Tunable Doping in High-Performance WSe_2 Devices. *Adv. Electron. Mater.* **2020**, *6*, 1901304.

(95) Shen, P.-C.; Su, C.; Lin, Y.; Chou, A.-S.; Cheng, C.-C.; Park, J.-H.; Chiu, M.-H.; Lu, A.-Y.; Tang, H.-L.; Tavakoli, M. M.; Pitner, G.; Ji, X.; Cai, Z.; Mao, N.; Wang, J.; Tung, V.; Li, J.; Bokor, J.; Zettl, A.; Wu, C.-I.; Palacios, T.; Li, L.-J.; Kong, J. Ultralow Contact Resistance between Semimetal and Monolayer Semiconductors. *Nature* **2021**, *593*, 211−217.

(96) Dong, H.; Gong, C.; Addou, R.; McDonnell, S.; Azcatl, A.; Qin, X.; Wang, W.; Wang, W.; Hinkle, C. L.; Wallace, R. M. Schottky Barrier Height of Pd/MoS_2 Contact by Large Area Photoemission Spectroscopy. *ACS Appl. Mater. Interfaces* **2017**, *9*, 38977−38983.

https://doi.org/10.1021/acsnano.3c06494
ACS Nano XXXX, XXX, XXX−XXX

(97) Wang, Y.; Chhowalla, M. Making Clean Electrical Contacts on 2D Transition Metal Dichalcogenides. *Nat. Rev. Phys.* **2022**, *4*, 101−112.

(98) Wang, Y.; Kim, J. C.; Li, Y.; Ma, K. Y.; Hong, S.; Kim, M.; Shin, H. S.; Jeong, H. Y.; Chhowalla, M. P-Type Electrical Contacts for Two-Dimensional Transition Metal Dichalcogenides. *Nature* **2022**, *610*, 61−66.

(99) Jain, A.; Ong, S. P.; Hautier, G.; Chen, W.; Richards, W. D.; Dacek, S.; Cholia, S.; Gunter, D.; Skinner, D.; Ceder, G.; Persson, K. A. Commentary: The Materials Project: A Materials Genome Approach to Accelerating Materials Innovation. *APL Mater.* **2013**, *1*, 011002.

(100) Lin, Y. *Advanced Nano Deposition Methods*; Wiley: 2016.

(101) Lunk, H.-J.; Hartl, H. Discovery, Properties and Applications of Tungsten and Its Inorganic Compounds. *ChemTexts* **2019**, *5*, 15.

(102) Bashir, A.; Awan, T. I.; Tehseen, A.; Tahir, M. B.; Ijaz, M. Chapter 3 - Interfaces and Surfaces. In *Chemistry of Nanomaterials*; Elsevier, 2020; pp 51−87.

(103) Deslattes, R. D.; Jr, E. G. K.; Indelicato, P.; Billy, L. d.; Lindroth, E.; Anton, J.; Coursey, J. S.; Schwab, D. J.; Chang, C.; Sukumar, R.; Olsen, K.; Dragoset, R. A. *X-Ray Transition Energies (Version 1.2)*. National Institute of Standards and Technology, Gaithersburg, MD., 2005.

(104) Burek, G. J.; Hwang, Y.; Carter, A. D.; Chobpattana, V.; Law, J. J. M.; Mitchell, W. J.; Thibeault, B.; Stemmer, S.; Rodwell, M. J. W. Influence of Gate Metallization Processes on the Electrical Characteristics of High-k/$In_{0.53}Ga_{0.47}As$ Interfaces. *J. Vac. Sci. Technol. B* **2011**, *29*, 040603.

(105) Chen, C.-H.; Hu, E. L.; Schoenfeld, W. V.; Petroff, P. M. Metallization-Induced Damage in III-V Semiconductors. *J. Vac. Sci. Technol. B* **1998**, *16*, 3354.

(106) Li, M.-Y.; Hsu, C.-H.; Shen, S.-W.; Chou, A.-S.; Lin, Y. C.; Chuu, C.-P.; Yang, N.; Chou, S.-A.; Huang, L.-Y.; Cheng, C.-C.; Woon, W.-Y.; Liao, S.; Wu, C.-I.; Li, L.-J.; Radu, I.; Wong, H.-S. P.; Wang, H., Wafer-Scale Bi-Assisted Semi-Auto Dry Transfer and Fabrication of High-Performance Monolayer CVD WS_2 Transistor. In *2022 IEEE Symposium on VLSI Technology and Circuits (VLSI Technology and Circuits)*; IEEE: 2022; pp 290−291.

(107) Honig, R. E. *Vapor Pressure Data for the More Common Elements*; David Sarnoff Research Center: Radio Corporation of America. RCA Labratories Division, 1957.

(108) Coelho, S. M. M.; Archilla, J. F. R.; Auret, F. D.; Nel, J. M. The Origin of Defects Induced in Ultra-Pure Germanium by Electron Beam Deposition. In *Quodons in Mica*; Springer International Publishing, 2015; pp 363−380.

(109) Yamada, M.; Matsumura, M.; Maeda, Y. Electron Beam Deposition System Causing Little Damage to Organic Layers. *Thin Solid Films* **2011**, *519*, 6219−6223.

(110) Martín-Palma, R. J.; Lakhtakia, A. Chapter 15 - Vapor-Deposition Techniques. In *Engineered Biomimicry*; Elsevier, 2013; pp 383−398.

(111) HQ Graphene. www.hqgraphene.com (accessed 15 September 2023).

(112) Wallace, R. M. In-Situ Studies of Interfacial Bonding of High-K Dielectrics for Cmos Beyond 22nm. *ECS Trans.* **2008**, *16*, 255−271.

(113) The University of Texas at Dallas Cleanroom https://cleanroom.utdallas.edu/ (Accessed 15 September 2023).

(114) ASTM E2108−16. *Standard Practice for Calibration of the Electron Binding Energy Scale of an X-Ray Photoelectron Spectrometer* 2016 (West Conshohocken, PA: ASTM) DOI: 10.1520/E2108-16.

(115) Herrera-Gómez, A.; Hegedus, A.; Meissner, P. L. Chemical Depth Profile of Ultrathin Nitrided Sio_2 Films. *Appl. Phys. Lett.* **2002**, *81*, 1014−1016.

(116) Horcas, I.; Fernández, R.; Gómez-Rodríguez, J. M.; Colchero, J.; Gómez-Herrero, J.; Baro, A. M. WSxM: A Software for Scanning Probe Microscopy and a Tool for Nanotechnology. *Rev. Sci. Instrum.* **2007**, *78*, 013705.

(117) Nečas, D.; Klapetek, P. Gwyddion: An Open-Source Software for SPM Data Analysis. *Open Physics* **2012**, *10*, 181−188.

(118) Kresse, G.; Furthmüller, J. Efficiency of Ab-Initio Total Energy Calculations for Metals and Semiconductors Using a Plane-Wave Basis Set. *Comput. Mater. Sci.* **1996**, *6*, 15−50.

(119) Kresse, G.; Hafner, J. Ab Initio Molecular Dynamics for Liquid Metals. *Phys. Rev. B* **1993**, *47*, 558−561.

(120) Kresse, G.; Hafner, J. Norm-Conserving and Ultrasoft Pseudopotentials for First-Row and Transition Elements. *J. Phys.: Condens. Matter* **1994**, *6*, 8245.

(121) Kresse, G.; Joubert, D. From Ultrasoft Pseudopotentials to the Projector Augmented-Wave Method. *Phys. Rev. B* **1999**, *59*, 1758−1775.

(122) Perdew, J. P.; Chevary, J. A.; Vosko, S. H.; Jackson, K. A.; Pederson, M. R.; Singh, D. J.; Fiolhais, C. Atoms, Molecules, Solids, and Surfaces: Applications of the Generalized Gradient Approximation for Exchange and Correlation. *Phys. Rev. B* **1992**, *46*, 6671.

(123) Perdew, J. P.; Burke, K.; Ernzerhof, M. Generalized Gradient Approximation Made Simple. *Phys. Rev. Lett.* **1996**, *77*, 3865.

https://doi.org/10.1021/acsnano.3c06494
ACS Nano XXXX, XXX, XXX−XXX